

論文 / 著書情報  
Article / Book Information

Title	Realization of a Bulk-Insulating Ferromagnetic Topological Crystalline Insulator and Its Multicarrier Surface Dirac-Cone Transport
Authors	Yoshihiro Fukushima, Satoru Ichinkura, Taisuke Sasaki, Toru Hirahara
Citation	Physical Review Letters, volume 136, issue 6, page 066602
Pub. date	2026, 2
Pub. version	<a href="https://doi.org/10.1103/wrpq-17h9">https://doi.org/10.1103/wrpq-17h9</a>
Copyright	(C) 2026 American Physical Society
Note	This file is author (final) version.

# Realization of a bulk-insulating ferromagnetic topological crystalline insulator and its multi-carrier surface Dirac-cone transport

Yoshihiro Fukushima<sup>1,\*</sup>, Satoru Ichinkura<sup>1,2</sup>, Taisuke Sasaki<sup>3</sup>, Toru Hirahara<sup>1,†</sup>

<sup>1</sup> Department of Physics, Institute of Science Tokyo, 152-8551 Tokyo, Japan

<sup>2</sup> Center for Basic Research on Materials, National Institute for Materials Science, 305-0003 Ibaraki, Japan

<sup>3</sup> Research Center for Magnetic and Spintronic Materials, National Institute for Materials Science, 305-0047 Ibaraki, Japan

**ABSTRACT.** We succeeded in fabricating an ideal, bulk insulating ferromagnetic topological crystalline insulator by doping Mn to SnTe films grown on Bi<sub>2</sub>Te<sub>3</sub>. The cancellation of the polarity of SnTe surface and electron doping due to Bi and Mn leads to an ideal case where only the electron and holes of topological surface Dirac carriers exist at the Fermi level in different region of the surface Brillouin zone and their competition results in a nonlinear Hall effect. Ferromagnetism has been confirmed at 3.5 K through the detection of the anomalous Hall effect. These properties can potentially serve to realize and manipulate the high-Chern number quantum anomalous Hall effect.

The combination of out-of-plane ferromagnetism and topology results in the realization of the quantum anomalous Hall effect (QAHE), in which the Hall resistance is quantized as at zero field,  $\rho_{xy} = \frac{h}{ce^2}$ , where  $h$  is the Planck constant,  $e$  is the elementary charge, and  $C$  is the Chern number. It was first verified in 2013 in Cr-doped BiSbTe [1] and then in various materials including intrinsic magnetic topological insulator (TI) MnBi<sub>2</sub>Te<sub>4</sub> [2] or twisted bilayer graphene [3]. Recently, some works have reported QAHE for  $|C| > 1$ , such as  $C=2$  for twisted monolayer-bilayer graphene [4]. The high-Chern number QAHE has also been proven by growing multilayers of  $C = 1$  QAH insulators and normal insulators. For example, in the Cr, V-codoped BiSbTe/CdSe multilayers [5] and CrBiSbTe/BiSbTe multilayers [6],  $C = 4$  and  $C = 5$  have been reported, respectively. However, the need to fabricate complex structures with high precision is a barrier. Furthermore, the value of  $|C|$ , thus the number of the chiral edge channels, cannot be manipulated easily within the same sample and this greatly limits the practical application of the high-Chern number QAHE in electronic devices.

An interesting material in this aspect is topological crystalline insulators (TCI). It was first proposed in 2011 [7] and experimentally verified next year for SnTe [8]. Multiple Dirac cones exist for various SnTe surfaces such as the (001), (110), and (111) and it has been predicted that any Chern number between  $\pm 4$  is possible when ferromagnetism is induced. It is also shown that  $C$  can be manipulated with electric field for the same sample [9]. However, although the effect of inducing magnetism in SnTe has been investigated [10-13], its relation to the electronic structure in SnTe has not been thoroughly studied. Especially, we would like to emphasize that there have been no reports up to now that have shown both

bulk insulating and ferromagnetic properties in TCI SnTe. Furthermore, since SnTe is a polar material, surface reconstruction and the existence of non-topological surface states have been reported from calculation [14-16]. However, such evidence has not been verified in experiments, and further study is needed to elucidate this apparent mystery.

Therefore, in the present study, we have doped Mn into SnTe films grown on Bi<sub>2</sub>Te<sub>3</sub> and performed *in situ* angle-resolved photoemission spectroscopy (ARPES) and Hall measurements for the same samples. The atomic structure was also characterized with scanning transmission electron microscopy (STEM). An ideal bulk insulating SnTe is realized with only the electron and hole Dirac surface states crossing the Fermi level  $E_F$  due to the effect of the Bi and Mn atoms. Consequently, a nonlinear Hall effect is observed which can be explained as a competition between the electron and hole carriers at the surface. A hysteresis loop was also observed at 3.5 K, showing that the system is ferromagnetic. This shows that these Mn-doped SnTe films can potentially be interesting to realize high-Chern number QAHE and control the edge channel by applying strain or electric fields.

SnTe films as well as two types of Mn-doped SnTe samples were prepared: the sample with lower Mn concentration is termed Mn(2ML)-SnTe, and the sample with higher Mn concentration is termed Mn(4ML)-SnTe. The experimental details can be found in the Supplementary Material [17]. First, we focus on the atomic structure of the grown samples. Figure 1(a) shows a large-scale high-Angle Annular Dark Field (HAADF) STEM image of the SnTe film, underlying Bi<sub>2</sub>Te<sub>3</sub>, the Te capping layer, and the Si substrate. The inset shows element specific image of images of Bi, Te and Sn at the SnTe surface measured with energy-dispersive X-ray spectroscopy

\*Contact author: fukushima@surfnano.phys.sci.isct.ac.jp

† Contact author: hirahara@phys.sci.isct.ac.jp

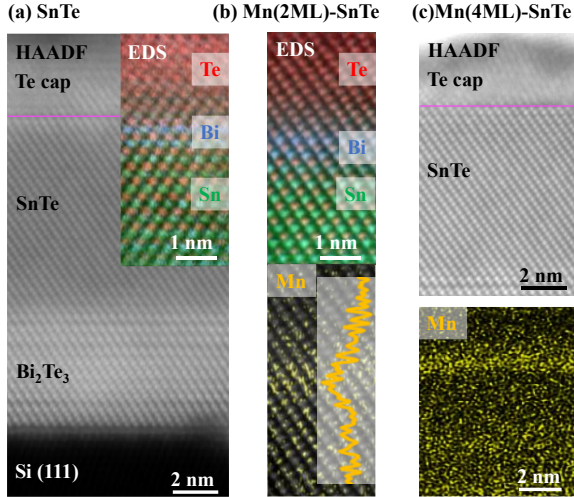


FIG 1. (a) Large-scale HAADF image of the SnTe film grown on  $\text{Bi}_2\text{Te}_3$ . The Si(111) substrate and the Te capping layer is also shown together with the boundary between the film and the capping layer. The inset shows the element-resolved magnified image near the film/capping layer interface. (b) Element-resolved magnified image near the film/capping layer interface for the Mn(2ML)-SnTe sample. (c) Large-scale HAADF image of the Mn(4ML)-SnTe sample, and the EDS mapping of Mn.

(EDS). One can notice that the films are terminated with Te layers but Bi atoms segregate to the SnTe surface from the  $\text{Bi}_2\text{Te}_3$  underneath. Figure 1(b) shows the element specific EDS image of the Mn(2ML)-SnTe sample surface showing the position of the Te, Bi, Sn, and Mn atoms. The distribution of Te, Bi and Sn atoms in Mn(2ML)-SnTe generally matches that of SnTe. Mn was shown to be particularly placed at the sample surface similar to Bi, but it also distributes inside the SnTe film. Figure 1(c) shows the large-scale HAADF STEM image for Mn(4ML)-SnTe, and like Mn(2ML)-SnTe, it shows that the distribution trend of Mn in Mn(4ML)-SnTe is concentrated near the sample surface although it is also found inside the SnTe film. Thus, we can say that the grown SnTe films are terminated with Bi and Mn at the surface, and Mn can also penetrate to the inner layers. Since SnTe is a polar material, the presence of electric field at the surface will make the system unstable and something to neutralize the charge polarity is needed. We believe that Bi acts as the main source of this polarity neutralization at the surface in the present case. As Mn is known to form  $\text{MnBi}_2\text{Te}_4$  when it is deposited onto  $\text{Bi}_2\text{Te}_3$  together with Te [23], it can naturally be understood that it will reside near the surface together with Bi. But since Mn and Te constitute MnTe, which has been

extensively investigated recently in the context of altermagnetism [24], it also seems reasonable that Mn can reside inside SnTe.

Now let us discuss how this structural change will influence the electronic properties of these SnTe films. Figure 2(a) shows the Fermi surface and Fig. 2(b) shows the band dispersion along the  $\bar{\Gamma}$ - $\bar{M}$  direction for the SnTe film (Fig. 2(i) is the surface Brillouin zone). The Fermi surface consists of a hexagonal feature around the  $\bar{\Gamma}$  point, needle like features along the  $\bar{\Gamma}$ - $\bar{M}$  direction, and an oval-shaped pocket around  $\bar{M}$ . The band dispersion near the  $\bar{\Gamma}$  point in Fig. 2(b) resembles that reported previously [25, 26] and likely consists of the bulk valence band together with the lower branch of the surface Dirac cone. A hole-like dispersion band can be found near the  $\bar{M}$  point in Fig. 2(b), and this should constitute the oval pocket and needle like features along  $\bar{\Gamma}$ - $\bar{M}$  in the Fermi surface. We believe that the band structure of SnTe can be schematically represented as shown in Fig. 2(j), adapted from the tight-binding calculations of Refs. [27] and [28] for the Te terminated SnTe slab. This fact shows that only the bulk bands and topological surface states are observed whereas the conventional surface states due to surface reconstruction or dangling bonds are absent, which have been predicted from first-principles calculations [14-16]. We think that this is a natural consequence of the Bi segregation to cancel the polarity at the surface and provides experimental evidence that the topological surface states are robust against surface decoration since their presence is guaranteed by the difference in topology between the vacuum (trivial insulator) and a topological insulator.

Figures 2(c) and (f) show the Fermi surface and the band dispersion along the  $\bar{\Gamma}$ - $\bar{M}$  direction for the Mn-doped SnTe(111) samples. In contrast to the complicated feature of Fig. 2(a) for pure SnTe, the Fermi surface is very simple composed of two circular pockets around  $\bar{\Gamma}$  and  $\bar{M}$ . From the band dispersion in Figs. 2(d) and (g), one can find that the former is an electron pocket and the latter a hole pocket. It can also be recognized that the band dispersion at  $\bar{\Gamma}$  seems to be a Dirac cone with linearly dispersing band near  $E_F$ , which is clearly shown in the band dispersion image deduced by dividing the raw data with the Fermi-Dirac distribution function (Figs. 2(e) and (h)). It should be emphasized that the linear band dispersion of the upper part of the Dirac cone is clearly observed above  $E_F$ . Thus, the band dispersion can most likely be schematically represented as shown in Fig. 2(k). In a simple picture, this band dispersion can be understood that electron doping has occurred compared to the non-Mn-doped SnTe sample of Figs. 2(b) and (j). Since the origin of

\*Contact author: fukushima@surfnano.phys.sci.isct.ac.jp

† Contact author: hirahara@phys.sci.isct.ac.jp

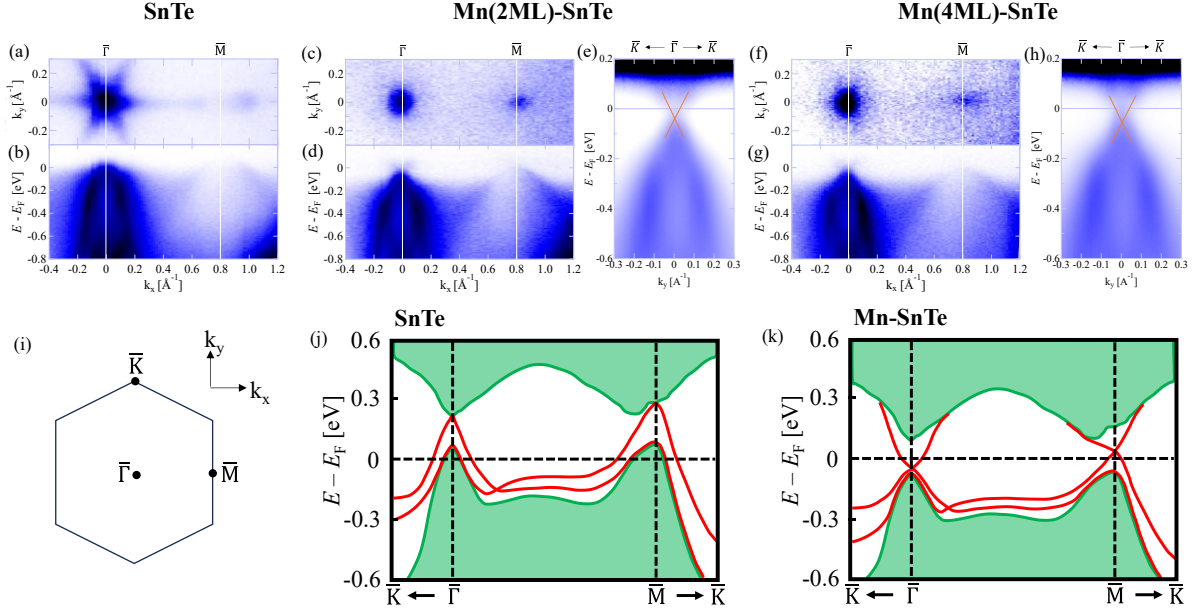


FIG 2. (a, b) Fermi surface (a) and band dispersion along the  $\bar{\Gamma}$ - $\bar{M}$  direction (b) of the SnTe(111) film, respectively. (c, d) Fermi surface (c) and band dispersion along the  $\bar{\Gamma}$ - $\bar{M}$  direction (d) of Mn(2ML)-SnTe, respectively. (e) Band dispersion along the  $\bar{\Gamma}$ - $\bar{K}$  direction of Mn(2ML)-SnTe. To enhance the features above  $E_F$ , the image has been divided by the Fermi-Dirac (FD) distribution function. (f, g) Fermi surface (f) and band dispersion along the  $\bar{\Gamma}$ - $\bar{M}$  direction (g) of Mn(4ML)-SnTe, respectively. (h) Band dispersion divided by the FD function along the  $\bar{\Gamma}$ - $\bar{K}$  direction of Mn(4ML)-SnTe. (i) Schematic drawing of the surface Brillouin zone of SnTe(111). (j) Schematic drawing of the band dispersion of a Te terminated SnTe(111) slab adapted from the tight-binding calculation of Refs. [27] and [28]. (k) Schematic drawing of the band dispersion of the Mn-doped samples in the present research.

hole-doping in SnTe is due to the presence of Sn deficiencies [29], we speculate that Mn atoms that are distributed inside the SnTe film fill the Sn defects and reduce the hole-doping and thus acts as an effective electron-doping. However, one needs to understand that the band shift is not proportional to the amount of Mn doping by comparing Figs. 2(d) and (g). Another important change is that although there is an overlap between the surface Dirac cone and the bulk valence/conduction band at the  $\bar{\Gamma}$  point which makes it impossible to access the surface electrons in the SnTe case (Fig. 2(j)), in the Mn-doped samples, the Dirac point as well as the upper branch of the Dirac cone seems to become isolated from the bulk bands (Fig. 2(k)). Therefore, although the reason is not clear, we can say that we have realized an ideal bulk insulating topological crystalline insulator with electron and hole pockets located at different regions of the surface Brillouin zone for the first time. Similar data has been obtained for other samples (Fig. S1 [17]).

It is important to see how this change in the electronic structure is reflected in the transport properties of the SnTe films. Figure 3(a) shows the temperature-dependent resistance (R-T) curve for

pure SnTe below 50 K [30]. It exhibits a metallic behavior, consistent with the metallicity of the bulk and surface states shown in Fig. 2(a) and (b). This behavior is also consistent with other reports on SnTe films [31,32]. In contrast, in the Mn-doped case, both Mn 2ML and 4 ML doped SnTe samples exhibit insulating behavior between 35 K and 50 K, and becomes nearly constant below 35 K. This behavior is similar to the bulk insulating conduction reported for a  $Z_2$  TI  $\text{Bi}_2\text{Te}_2\text{Se}$  [33] and consistent with the fact that only the surface-state Dirac cones cross the Fermi level in the band dispersion (Figs. 2(c) and (f)). Moreover, a simple thermal activation conduction model was used to separate the bulk and surface contributions, confirming that the low-temperature (below 35 K) transport is dominated by the surface-state (Fig. S4 [17]).

To gain further insight, we have applied a magnetic field perpendicular to the surface and Figs. 3(d)–(f) show the magnetic field dependence of the rate of the change of longitudinal resistance from zero field ( $\Delta R_{xx}(B)/R_{xx}(0)$ ) at 3.5 K for the pure SnTe (d), Mn(2ML)-SnTe (e), and Mn(4ML)-SnTe (f), respectively. In Fig. 3(d), the large dip appearing near zero magnetic field is a characteristic of weak anti-

\*Contact author: fukushima@surfnano.phys.sci.isct.ac.jp

† Contact author: hirahara@phys.sci.isct.ac.jp

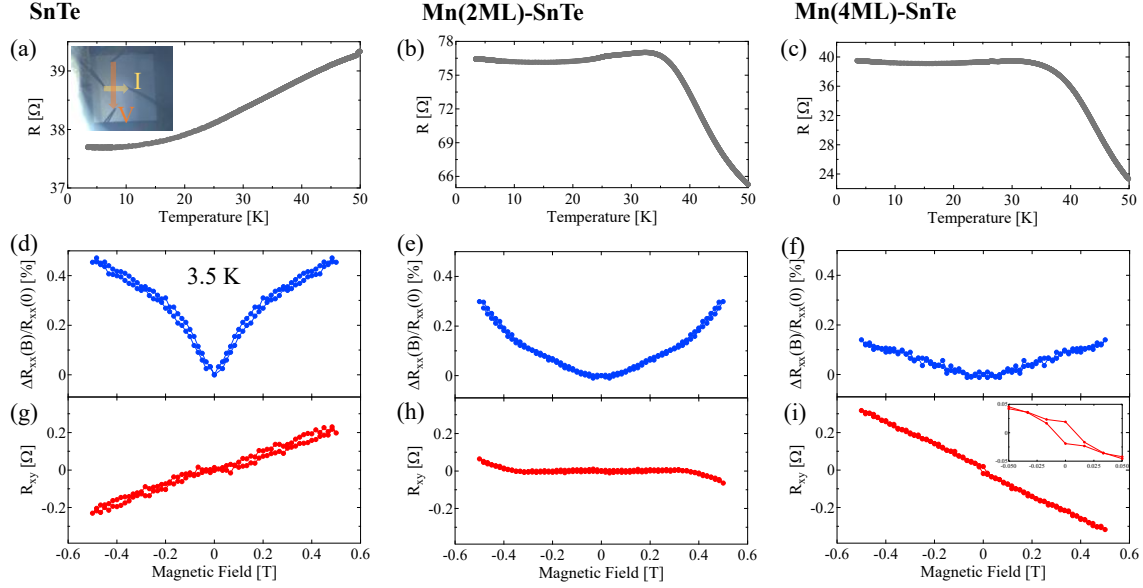


FIG 3. (a, b, c) Temperature dependence of the measured resistance ( $R$ ) for the SnTe(111) film (a), Mn(2ML)-SnTe (b), and Mn(4ML)-SnTe (c), respectively. (d, e, f) Magnetic-field dependence of rate of the change of  $R_{xx}$  ( $\Delta R_{xx}(B) (=R_{xx}(B) - R_{xx}(0))/R_{xx}(0)$ ) at 3.5 K for the SnTe(111) film (d), Mn(2ML)-SnTe (e), and Mn(4ML)-SnTe (f), respectively. (g, h, i) Magnetic-field dependence of the Hall resistance  $R_{xy}$  at 3.5 K for the SnTe(111) film (g), Mn(2ML)-SnTe (h), and Mn(4ML)-SnTe (i), respectively. The inset in (i) shows the observed hysteresis near zero-field.

localization (WAL) and has been reported previously for SnTe films [34–36]. The strong spin-orbit coupling leads to the destructive interference of wave functions at zero field and hence the resistance increases by applying a field. Figures 3(e) and (f) show that doping with Mn suppresses the WAL possibly due to the induced magnetism, as discussed later.

Figures 3(g)-(i) show the magnetic field dependence of the Hall resistance ( $R_{xy}$ - $B$ ) at 3.5 K for the pure SnTe (g), Mn(2ML)-SnTe (h), and Mn(4ML)-SnTe (i), respectively. The positive slope in Fig. 3(g) confirms that the carriers of SnTe are holes, consistent with previous studies [37] as well as the band dispersion of Fig. 2(b). In Fig. 3(i), a negative slope is observed, showing that the carriers become electrons by Mn doping as demonstrated by

ARPES. The most interesting Hall resistance curve is Fig. 3(h) for Mn(2ML)-SnTe, showing the nonlinear dependence to the magnetic field. It should be noted that by zooming in the data, a hysteresis loop can be observed both for Mn(2ML)-SnTe (Fig. 4(a)) and Mn(4ML)-SnTe (inset of Fig. 3(i)). This shows that the system becomes ferromagnetic by Mn doping at 3.5 K.

To analyze the nonlinear Hall resistance of Mn(2ML)-SnTe in more detail, we replot the data of Fig. 3(h) in Fig. 4(a) in a modified vertical axis range. One can obviously find that a negative slope is found for  $|B| > 0.4$  T whereas it is slightly positive with a hysteresis for  $|B| < 0.4$  T. This indicates a change in the carrier type. The temperature dependence of the nonlinear Hall resistance in Mn(2ML)-SnTe up to 20 K, is shown in Figs. 4(b)–

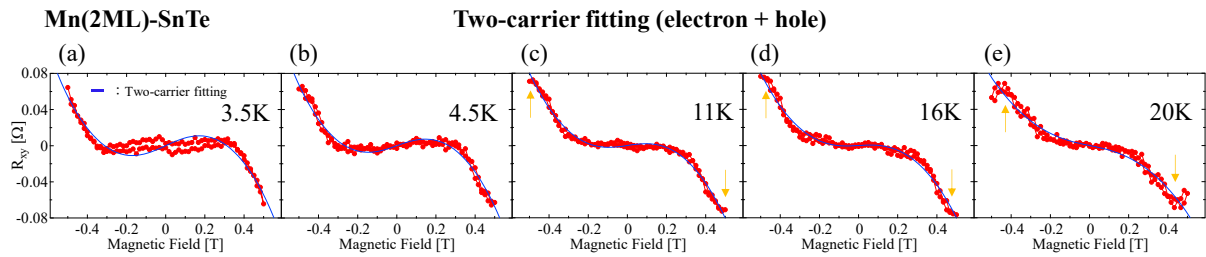


FIG 4. Temperature dependence of the Hall resistance of Mn(2ML)-SnTe measured at 3.5 K (a), 4.5 K (b), 11 K (c), 16 K (d), and 20 K (e), respectively. The blue lines show the result of the two-carrier fitting according to Eq. (1) and the arrows indicated the deviation from this model.

\*Contact author: fukushima@surfnano.phys.sci.isct.ac.jp

† Contact author: hirahara@phys.sci.isct.ac.jp

(e). The anomalous Hall signal already disappears at 4.5 K, showing that the Curie temperature is quite low. With further temperature increase, the gradient of the Hall resistance near zero field changes from positive to negative and a change in the curvature appears at high magnetic fields as shown by the arrows. It is especially noticeable at 20 K with a peak structure at  $\sim \pm 0.45$  T.

Since the electronic structure of Mn-doped SnTe possesses surface-state Fermi surfaces at the  $\bar{\Gamma}$  and  $\bar{M}$  points, the nonlinear Hall effect observed in Fig. 4 may be attributed to the complex cooperation or competition of multiple carriers contributing to the conduction. Therefore, the experimental data were fitted using Eq. (1), which considers two types of carriers (electrons and holes) [38]:

$$R_H = -\frac{1}{B_Z} \frac{B_1 - B_2}{(A_1 + A_2)^2 + (B_1 - B_2)^2} \quad (1)$$

where  $B_Z$  is the value of the applied magnetic field and

$$A_i = \frac{en_i\mu_i}{1+(\mu_i B_Z)^2}, B_i = \frac{en_i\mu_i^2 B_Z}{1+(\mu_i B_Z)^2} \quad (i = 1, 2 \text{ for electrons and holes, respectively}).$$

The parameters  $n_i$  and  $\mu_i$  are the carrier density and the mobility of the carriers. The fitted results are plotted as blue lines in Figs. 4(a)–(e) and the deduced parameters are shown in TABLE I. The carrier density shows almost no temperature dependence, and the order of magnitude is consistent with the carrier density calculated from the Fermi surface at room temperature (Fig. 2(c)) [39]. Furthermore, the mobility values obtained were relatively high, consistent with those expected to originate from the Dirac surface-states. Thus, we believe that the observed non-linear Hall resistance is a result of the multi-carrier transport of the Dirac electrons and holes in this system. This cannot be realized in conventional  $Z_2$  TI with a single Dirac-cone surface state and is a novel finding.

We also note that while these fitting results show satisfactory agreement below 11 K showing the change of the slope at high and low fields, the cusp-like (or dip-like) feature at high fields indicated by the arrows is not reproduced. We have therefore tried to reproduce this feature by adding another carrier, namely the bulk holes, to Eq. (1) and performed the fitting. This, however, did not give satisfactory results and is also not consistent with the fact that bulk carriers should have frozen out below 30 K as was shown in Fig. 3(b). While the origin of this peculiar behavior cannot be directly identified now, a plausible explanation may be that there is another type of Hall effect arising, namely the topological Hall effect due to skyrmion formation. It has been suggested in Ref. [40] that skyrmions can start to form at lower magnetic field when the temperature is increased for  $Gd_2PdSi_3$ . Since the Mn atoms are localized at the surface, the Dzyaloshinskii-Moriya interaction may play a role to create skyrmions in this system. As this anomaly is only clearly observed

at 20 K, applying higher fields may help to clarify the real situation.

TABLE I. Carrier Density and Mobility obtained from the two-carrier fitting and ARPES for Mn(2ML)-SnTe.

	Two-carrier fitting					ARPES
	3.5K	4.5K	11K	16K	20K	Fermi surface
Electrons $n_1$ [cm <sup>-2</sup> ]	$6.0 \times 10^{13}$	$5.8 \times 10^{13}$	$5.8 \times 10^{13}$	$5.7 \times 10^{13}$	$5.9 \times 10^{13}$	$3.5 \times 10^{13}$
$\mu_1$ [cm <sup>2</sup> /Vs]	$5.5 \times 10^3$	$5.6 \times 10^3$	$5.4 \times 10^3$	$5.5 \times 10^3$	$4.9 \times 10^3$	-
Holes $n_2$ [cm <sup>-2</sup> ]	$3.4 \times 10^{13}$	$3.4 \times 10^{13}$	$3.5 \times 10^{13}$	$3.5 \times 10^{13}$	$3.8 \times 10^{13}$	$3.3 \times 10^{13}$
$\mu_2$ [cm <sup>2</sup> /Vs]	$7.4 \times 10^3$	$7.4 \times 10^3$	$7.0 \times 10^3$	$7.0 \times 10^3$	$5.7 \times 10^3$	-

We can say that we have experimentally demonstrated for the first time that, when polarity is cancelled due to Bi and Mn segregation at the surface of SnTe, the conventional surface states disappear, leaving only topological surface states at  $E_F$ , thereby realizing a bulk insulating, multi-carrier Dirac system. Furthermore, the system becomes ferromagnetic. This shows the successful combination of topology and magnetism with multiple carriers in a rather simple setup. It suggests the potential for a new Chern number-controlled QAHE by applying strain, which goes beyond the conventional QAHE where the Chern number is  $\pm 1$ . All the measurements in this study were conducted in-situ with low magnetic field. Future experiments on Shubnikov-de Haas (SdH) oscillations at high-magnetic-field can further confirm the underlying physics picture.

In summary, doping of the topological crystal insulator SnTe with Mn, fabricated on  $Bi_2Te_3$ , successfully demonstrated the two prerequisites for the QAHE: bulk insulating properties and out-of-plane ferromagnetism. Results from both ARPES and Hall measurements confirm that the transport properties originate from surface states. This work provides the first experimental demonstration of a bulk insulating multi-carrier Dirac surface-state system in a TCI, paving the way for the realization of a high-Chern-number QAHE in a simple setup.

## ACKNOWLEDGMENTS

We thank S. V. Eremeev for stimulating discussions. This work was supported by JST SPRING, Japan Grant Number JPMJSP2180. T.H. acknowledges the support by Grants-In-Aid from Japan Society for the Promotion of Science (Grants No. 18H03877, No. 22H00293, and No. 23H00268), the Murata Science Foundation (Grant No. H30084), the Asahi Glass Foundation, the Iketani Science and Technology Foundation (Grant No. 0321083-A), and Support for Tokyo Tech Advanced Researchers.

\*Contact author: fukushima@surfnano.phys.sci.isct.ac.jp

† Contact author: hirahara@phys.sci.isct.ac.jp

- [1] C.-Z. Chang, J. Zhang, X. Feng, J. Shen, Z. Zhang, M. Guo, K. Li, Y. Ou, P. Wei, L.-L. Wang, Z. -Q. Ji, Y. Feng, S. Ji, X. Chen, J. Jia, X. Dai, Z. Fang, S.-C. Zhang, K. He, Y. Wang, L. Lu, X.-C. Ma, Q.-K. Xue, Experimental Observation of the Quantum Anomalous Hall Effect in a Magnetic Topological Insulator, *Science* **340**, 167 (2013).
- [2] Y. Deng, Y. Yu, M. Z. Shi, Z. Guo, Z. Xu, J. Wang, X. H. Chen, Y. Zhang, Quantum anomalous Hall effect in intrinsic magnetic topological insulator  $\text{MnBi}_2\text{Te}_4$ , *Science* **367** 895 (2020).
- [3] M. Serlin, C. L. Tschirhart H. Polshyn, Y. Zhang, J. Zhu, K. Watanabe, T. Taniguchi, L. Balents, and A. F. Young, Intrinsic quantized anomalous Hall effect in a moiré heterostructure, *Science* **367** 900 (2020).
- [4] H. Polshyn, J. Zhu, M. A. Kumar, Y. Zhang, F. Yang, C. L. Tschirhart, M. Serlin, K. Watanabe, T. Taniguchi, A. H. MacDonald, and A. F. Young, Electrical switching of magnetic order in an orbital Chern insulator, *Nature* **588**, 66 (2020).
- [5] G. Jiang, Y. Feng, W. Wu, S. Li, Y. Bai, Y. Li, Q. Zhang, L. Gu, X. Feng, D. Zhang, C. Song, L. Wang, W. Li, X.-C. Ma, Q.-K. Xue, Y. Wang, K. He, Quantum Anomalous Hall Multilayers Grown by Molecular Beam Epitaxy, *Chin. Phys. Lett.* **35**, 076802 (2018).
- [6] Y.-F. Zhao, R. Zhang, R. Mei, L.-J. Zhou, H. Yi, Y.-Q. Zhang, J. Yu, R. Xiao, K. Wang, N. Samarth, M. H. W. Chan, C.-X. Liu, C.-Z. Chang, Tuning the Chern number in quantum anomalous Hall insulators, *Nature* **588**, 419 (2020).
- [7] L. Fu, Topological Crystalline Insulators, *Phys. Rev. Lett.* **106**, 106802 (2011).
- [8] Y. Tanaka, Z. Ren, T. Sato, K. Nakayama, S. Souma, T. Takahashi, K. Segawa, and Y. Ando, Experimental realization of a topological crystalline insulator in SnTe, *Nat. Phys.* **8**, 800 (2012).
- [9] C. Fang, M. J. Gilbert, B. A. Bernevig, Large-Chern-Number Quantum Anomalous Hall Effect in Thin-Film Topological Crystalline Insulators, *Phys. Rev. Lett.* **112**, 046801 (2014).
- [10] R. Akiyama, R. Ishikawa, K. Akutsu-Suyama, R. Nakanishi, Y. Tomohiro, K. Watanabe, K. Iida, M. Mitome, S. Hasegawa, and S. Kuroda, Direct probe of ferromagnetic proximity effect at the interface in SnTe/Fe heterostructure by polarized neutron reflectometry, *J. Phys. Chem. Lett.* **13**, 8228 (2022).
- [11] A.J.Nadolnya, J.Sadowskia, B.Taliashvilia, M.Arciszewskaa, W.Dobrowolskia, V.Domukhovskia, E. Łusakowskaa, A. Mycielskia, V. Osinniya, T. Storya, K. Swiateka, R.R. Galazkaa, and R. Diduszkob, Carrier induced ferromagnetism in epitaxial  $\text{Sn}_{1-x}\text{Mn}_x\text{Te}$  layers, *Jour. Mag. Mag. Mat.* **248**, 134 (2002).
- [12] F. Wang, H. Zhang, J. Jiang, Y.F. Zhao, J. Yu, W. Liu, D. Li, M. H. W. Chan, J. Sun, Z. Zhang, C. Z. Chang, Chromium-induced ferromagnetism with perpendicular anisotropy in topological crystalline insulator SnTe (111) thin films, *Phys. Rev. B* **97**, 115414 (2018).
- [13] R. Adhikari, V. V. Volobuev, B. Faina, G. Springholz, A. Bonanni, Ferromagnetic phase transition in topological crystalline insulator thin films: Interplay of anomalous Hall angle and magnetic anisotropy, *Phys. Rev. B* **100**, 134422 (2019).
- [14] S. V. Eremeev, Yu. M. Koroteev, I. A. Nechaev, and E. V. Chulkov, Role of surface passivation in the formation of Dirac states at polar surfaces of topological crystalline insulators: The case of SnTe(111), *Phys. Rev. B* **89**, 165424 (2014).
- [15] J. Wang, J. Liu, Y. Xu, J. Wu, B.-L. Gu, W. Duan, Structural stability and topological surface states of the SnTe (111) surface, *Phys. Rev. B* **89**, 125308 (2014).
- [16] Y. Shi, M. Wu, F. Zhang, J. Feng. (111) surface states of SnTe, *Phys. Rev. B* **90**, 235114 (2014).
- [17] See Supplemental Material [url] for the experimental details, reproducibility of [the Mn(2, 4 ML)–SnTe sample fabrication from ARPES measurements, extraction of  $R_{xx}$  and  $R_{xy}$  from the raw data, and the separation of bulk conduction and surface-state transport using the thermal activation conduction model.], which includes Refs. [18-22].
- [18] S. Fragkos, R. Sant, C. Alvarez, E. Golias, J. M. Velasco, P. Tsipas, D. Tsoutsou, S. A.-Giamini, E. Xenogiannopoulou, H. Okuno, G. Renaud, O. Rader, A. Dimoulas, “Topological band crossings in epitaxial strained SnTe”, *Phys. Rev. Mater* **3**, 104201 (2019).
- [19] A. K. Pedersen, S. Ichinokura, T. Tanaka, R. Shimizu, T. Hitosugi, and T. Hirahara, Interfacial superconductivity in FeSe ultrathin films on SrTiO<sub>3</sub> probed by in situ independently driven four-point-probe measurements, *Phys. Rev. Lett.* **124**, 227002 (2020).
- [20] K. Ide, T. Tanaka, A. Pedersen, S. Ichinokura, and T. Hirahara, Temperature dependence of the superconducting gap of single-layer FeSe/SrTiO<sub>3</sub>: Direct comparison between transport and spectroscopic measurements, *Phys. Rev. Mater.* **6**, 124801 (2022).
- [21] K. Ishihara, S. Ichinokura, S. V. Eremeev, T. T. Sasaki, R. Takada, H. Nishimichi, R. Akiyama, E. V. Chulkov, and T. Hirahara, Manipulation of the anomalous Hall effect in magnetic topological insulator heterostructure  $\text{MnBi}_2\text{Te}_4/\text{Bi}_2\text{Te}_3$  by Si

\*Contact author: fukushima@surfnano.phys.sci.isct.ac.jp

† Contact author: hirahara@phys.sci.isct.ac.jp

- substrate surface engineering, *Appl. Phys. Lett.* **127**, 211601 (2025).
- [22] G. Bergmann, Weak localization in thin films: a time-of-flight experiment with conduction electrons, *Phys. Rep.* **107**, 1 (1984).
- [23] T. Fukasawa, S. Kusaka, K. Sumida, M. Hashizume, S. Ichinokura, Y. Takeda, S. Ideta, K. Tanaka, R. Shimizu, T. Hitosugi, and T. Hirahara, Absence of ferromagnetism in  $\text{MnBi}_2\text{Te}_4/\text{Bi}_2\text{Te}_3$  down to 6 K, *Phys Rev B* **103**, 205405 (2021).
- [24] S. Lee, S. Lee, S. Jung, J. Jung, D. Kim, Y. Lee, B. Seok, J. Kim, B. G. Park, L. Šmejkal, C.-J. Kang, and C. Kim, Broken Kramers Degeneracy in Altermagnetic MnTe, *Phys Rev Lett.* **132**, 036702 (2024).
- [25] Y. Tanaka, T. Shoman, K. Nakayama, S. Souma, T. Sato, T. Takahashi, M. Novak, K. Segawa, Y. Ando, Two types of Dirac-cone surface states on the (111) surface of the topological crystalline insulator SnTe, *Phys. Rev. B* **88**, 235126 (2013).
- [26] C. Yan, J. Liu, Y. Zang, J. Wang, Z. Wang, P. Wang, Z. D. Zhang, L. Wang, X. Ma, S. Ji, K He, L. Fu, W. Duan, Q. K. Xue, X. Chen, Experimental Observation of Dirac-like Surface States and Topological Phase Transition in  $\text{Pb}_{1-x}\text{Sn}_x\text{Te}$  (111) Films, *Phys. Rev. Lett.* **112**, 186801 (2014).
- [27] S. Safaei, P. Kacman, R. Buczko, Topological crystalline insulator (Pb,Sn)Te: Surface states and their spin polarization, *Phys. Rev. B* **88**, 045305 (2013).
- [28] J. Liu, W. Duan, L. Fu, Two types of surface states in topological crystalline insulators, *Phys. Rev. B* **88**, 241303(R) (2013).
- [29] G. Tan, L.-D. Zhao, F. Shi, J. W. Doak, S.-H. Lo, H. Sun, C. Wolverton, V. P. Dravid, C. Uher, and M. G. Kanatzidis, High thermoelectric performance of p-type SnTe via a synergistic band engineering and nanostructuring approach, *J. Am. Chem. Soc.* **136**, 7006 (2014).
- [30] Although both the longitudinal and Hall resistance is included in the measured  $R$ , it basically reflects  $R_{xx}$  as shown in Figs. S2 and S3 [17].
- [31] A. A. Taskin, F. Yang, S. Sasaki, K. Segawa, Y. Ando, Topological surface transport in epitaxial SnTe thin films grown on  $\text{Bi}_2\text{Te}_3$ , *Phys. Rev. B* **89**, 121302(R) (2014).
- [32] S. Liu, E. Zhang, Z. Li, X. Zhang, W. Liu, A. Narayan, Z. G. Chen, J. Zou, F. Xiu, Cr doping-induced ferromagnetism in SnTe thin films, *npj Quantum Mater.* **9**, 57 (2024).
- [33] Z. Ren, A. A. Taskin, S. Sasaki, K. Segawa, and Y. Ando, Large bulk resistivity and surface quantum oscillations in the topological insulator  $\text{Bi}_2\text{Te}_2\text{Se}$ , *Phys. Rev. B* **82**, 241306(R) (2010).
- [34] H.Z. Lu, J. Shi, S. Q. Shen, Competition between Weak Localization and Antilocalization in Topological Surface States, *Phys. Rev. Lett.* **107**, 076801 (2011).
- [35] R. Akiyama, K. Fujisawa, T. Yamaguchi, R. Ishikawa, S. Kuroda, Two-dimensional quantum transport of multivalley (111) surface state in topological crystalline insulator SnTe thin films, *Nano Res* **9**, 490 (2016).
- [36] C. Zhang, Y. Liu, X. Yuan, W. Wang, S. Liang, F. Xiu, Highly Tunable Berry Phase and Ambipolar Field Effect in Topological Crystalline Insulator  $\text{Pb}_{1-x}\text{Sn}_x\text{Se}$ , *Nano Lett.* **15**, 2161 (2015).
- [37] P. Dziawa, B. J. Kowalski, K. Dybko, R. Buczko, A. Szczerbakow, M. Szot, E. Łusakowska, T. Balasubramanian, B. M. Wojek, M. H. Berntsen, O. Tjernberg, T. Story, Topological crystalline insulator states in  $\text{Pb}_{1-x}\text{Sn}_x\text{Se}$ , *Nat. Mater* **11**, 1023 (2012).
- [38] Jeffrey Lindemuth, Hall Effect Measurement Handbook (LakeShore CRYOTRONICS) [https://qdusa.com/siteDocs/productBrochures/Lake\\_Shore\\_Hall\\_Effect\\_Handbook.pdf](https://qdusa.com/siteDocs/productBrochures/Lake_Shore_Hall_Effect_Handbook.pdf)
- [39] We should note that since we have not fabricated a Hall bar structure,  $n_i$  deduced from the two-carrier fitting can only be compared qualitatively with the ARPES data.
- [40] T. Kurumaji, T. Nakajima, M. Hirschberger, A. Kikkawa, Y. Yamasaki, H. Sagayama, H. Nakao, Y. Taguchi, T. Arima, and Y. Tokura, Skyrmion lattice with a giant topological Hall effect in a frustrated triangular-lattice magnet, *Science* **365**, 914 (2019).

\*Contact author: fukushima@surfnano.phys.sci.isct.ac.jp

† Contact author: hirahara@phys.sci.isct.ac.jp

# Supplementary material for “Realization of a bulk-insulating ferromagnetic topological crystalline insulator and its multi-carrier surface Dirac-cone transport”

Yoshihiro Fukushima<sup>1,\*</sup>, Satoru Ichinkura<sup>1,2</sup>, Taisuke Sasaki<sup>3</sup>, Toru Hirahara<sup>1,†</sup>

<sup>1</sup> Department of Physics, Institute of Science Tokyo, 152-8551 Tokyo, Japan

<sup>2</sup> Center for Basic Research on Materials, National Institute for Materials Science, 305-0003 Ibaraki, Japan

<sup>3</sup> Research Center for Magnetic and Spintronic Materials, National Institute for Materials Science, 305-0047 Ibaraki, Japan

\* [fukushima@surfnano.phys.sci.isct.ac.jp](mailto:fukushima@surfnano.phys.sci.isct.ac.jp) † [hirahara@phys.sci.isct.ac.jp](mailto:hirahara@phys.sci.isct.ac.jp)

## I. Experimental

SnTe and Mn-doped SnTe were fabricated by molecular beam epitaxy (MBE) using a reflection high-energy electron diffraction (RHEED) system. Initially, a clean Si (111)- $7 \times 7$  surface was prepared on an n-type Si (111) substrate via a cycle of resistance heating. Bi was then directly deposited onto this  $7 \times 7$  surface under Te-rich conditions at approximately 200°C to grow a Bi<sub>2</sub>Te<sub>3</sub> thin film. The thickness of the material was monitored by RHEED oscillations. SnTe was fabricated by co-evaporating Sn and Te onto Bi<sub>2</sub>Te<sub>3</sub>/Si (111) substrates under Te-rich conditions. Subsequently, Mn and Te were co-evaporated onto SnTe(111) film to produce the Mn-doped SnTe samples, Mn(2ML)-SnTe and Mn(4ML)-SnTe. The in-plane lattice constant of the (111) surface of the prepared SnTe and Mn-doped SnTe samples was found to be 4.44 Å, which is consistent with the reported value [1].

ARPES measurements were performed in situ after sample preparation using a commercial hemispherical photoelectron spectrometer (Scienta Omicron R4000) equipped with multi-detector capabilities for both angle and energy. Measurements were performed at room temperature with He I $\alpha$  radiation (21.2 eV).

Then, transport measurements were performed in our custom-made system which has four probes that can move independently and by touching the surface of the sample, four-point probe (4PP) resistance measurements can be performed in ultrahigh vacuum [2-4]. In this study, the sample was cooled to approximately 3 K, and a magnetic field of up to 0.5 T was applied perpendicular to the sample surface. The longitudinal and Hall resistance was deduced as described in the next section.

The specimen was capped with approximately 10 nm of Te before its removal from the UHV chamber for scanning transmission electron microscopy (STEM) measurements. The electron-transparent specimen for STEM observation was prepared using a standard lift-out method with an FEI Helios G4-UX dual-beam system. A probe spherical aberration-corrected STEM instrument, the Thermo Fisher

Scientific Spectra Ultra, was used. Energy-dispersive X-ray spectroscopy (EDS) was employed for chemical composition measurements.

## II. Reproducibility of Mn-Doped SnTe thin-film growth

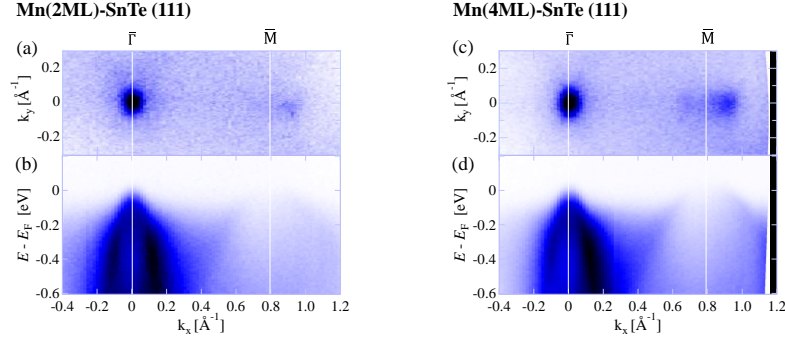


FIG. S1. (a, b) Fermi surface (a) and band dispersion along the  $\bar{\Gamma}$ - $\bar{M}$  direction (b) of Mn(2ML)-SnTe measured on a different sample from that used in the main text, respectively. (c, d) Fermi surface (c) and band dispersion along the  $\bar{\Gamma}$ - $\bar{M}$  direction (d) of Mn(4ML)-SnTe measured on a different sample from that used in the main text, respectively.

To verify the reproducibility of the samples used in this study, ARPES measurements were performed on separately prepared Mn(2ML)-SnTe and Mn(4ML)-SnTe samples. The obtained Fermi surfaces and band dispersions along the  $\bar{\Gamma}$ - $\bar{M}$  direction were in good agreement with the results presented in the main text, confirming the excellent reproducibility of the samples (see Fig. S1).

## III. Extraction of the Hall Resistance $R_{xy}$ and the longitudinal resistance $R_{xx}$ from the raw data

Figures S2(a)-(c) show the raw data  $R = V / I$  for the SnTe (a), Mn(2ML)-SnTe (b), and Mn(4ML)-SnTe (c) respectively, measured at  $\sim 3$  K. One can notice that there is slight asymmetry between the data points at positive and negative magnetic field due to the misalignment of the voltage probes. Therefore, the longitudinal resistance  $R_{xx}$  is deduced by symmetrizing the raw data [(d)-(f)] and the Hall resistance  $R_{xy}$  is derived by asymmetrizing the raw data [(g)-(i)], respectively.

By comparing Figs. S2(a), (d), and (g),  $R$  resembles  $R_{xx}$  rather than  $R_{xy}$ . Therefore, we can say that the temperature dependence of  $R$  for SnTe shown in Fig. 3(a) is reflecting the behavior of  $R_{xx}$ . The same holds for Mn(2ML)-SnTe in Fig. 3(b). The situation is a bit different for the Mn(4ML)-SnTe sample shown in Figs. S2(c), (f), and (g) and  $R$  resembles  $R_{xy}$  rather than  $R_{xx}$ . Therefore, we consider the temperature dependence of  $R_{xx}$  and  $R_{xy}$  in detail as shown in Fig. S3. One can see that the magnetic field dependence of  $R_{xx}$  diminishes with increasing temperature, while the slope of  $R_{xy}$  becomes  $\sim 2/3$  by raising the temperature to 20 K. This change is presumably due to a delicate balance between the transport of surface electrons and holes. The important point is that  $R_{xy}$  at zero field is nearly zero in Figs. S3(e)-(h) since the anomalous Hall signal seems to be absent above 4.5 K. Thus, we can safely say that

temperature dependence of  $R$  of Mn(4ML)-SnTe shown in Fig. 3(c) is reflecting the behavior of  $R_{xx}$  in this case too.

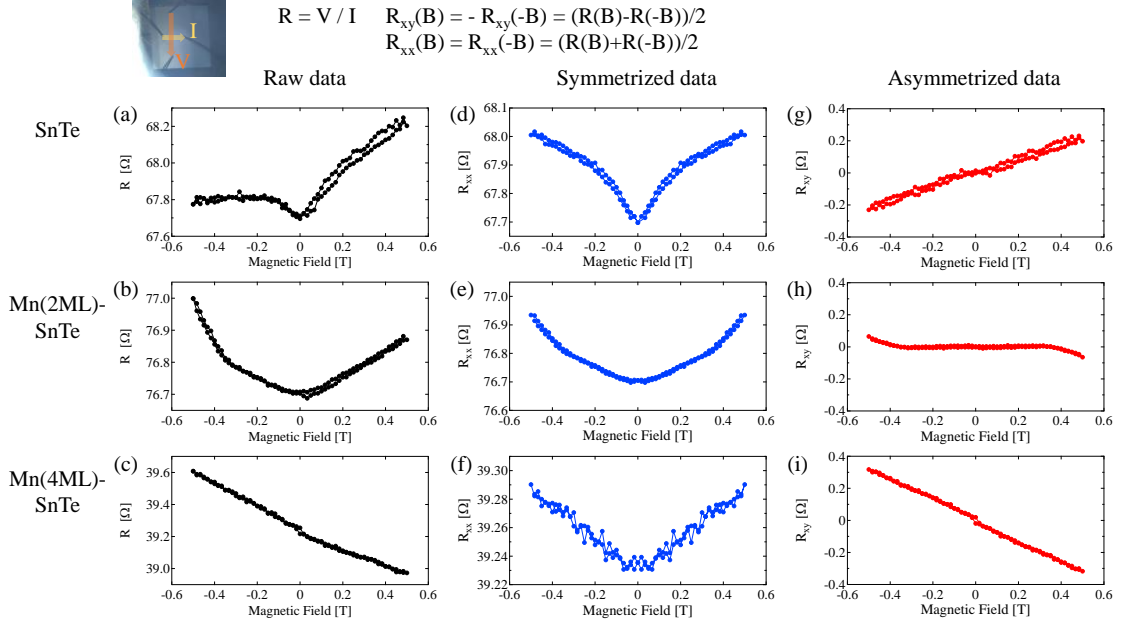


FIG S2. (a, b, c) Magnetic-field dependence of the measured resistance ( $R$ ) for the SnTe(111) film (a), Mn(2ML)-SnTe (b), and Mn(4ML)-SnTe (c), respectively, measured at 3.5 K. (d, e, f) Magnetic-field dependence of the longitudinal resistance  $R_{xx}$  derived by symmetrizing the raw data for the SnTe(111) film (d), Mn(2ML)-SnTe (e), and Mn(4ML)-SnTe (f), respectively. (g, h, i) Magnetic-field dependence of the Hall resistance  $R_{xy}$  derived by asymmetrizing the raw data for the SnTe(111) film (g), Mn(2ML)-SnTe (h), and Mn(4ML)-SnTe (i), respectively.

Mn(4ML)-SnTe

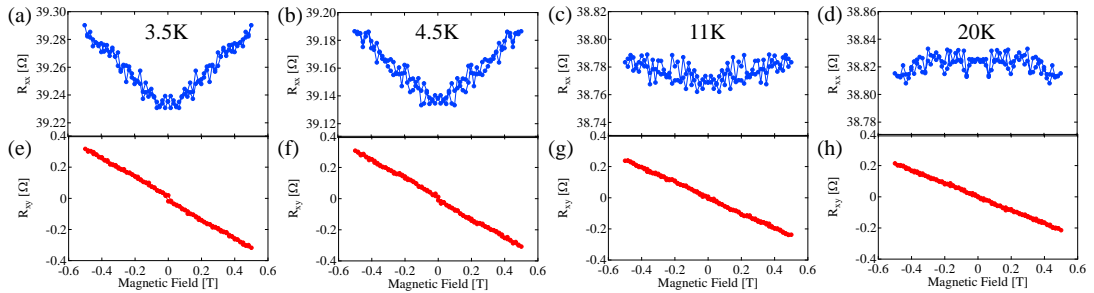


FIG S3. (a-d) Magnetic-field dependence of the longitudinal resistance  $R_{xx}$  derived by symmetrizing the raw data for the Mn(4ML)-SnTe at 3.5 K (a), 4.5 K (b), 11 K (c), and 20 K (d), respectively. (e-h) Magnetic-field dependence of the Hall resistance  $R_{xy}$  derived by asymmetrizing the raw data for the Mn(4ML)-SnTe at 3.5 K (e), 4.5 K (f), 11 K (g), and 20 K (h), respectively.

#### IV. Isolation of the bulk contribution in the temperature-dependent resistance

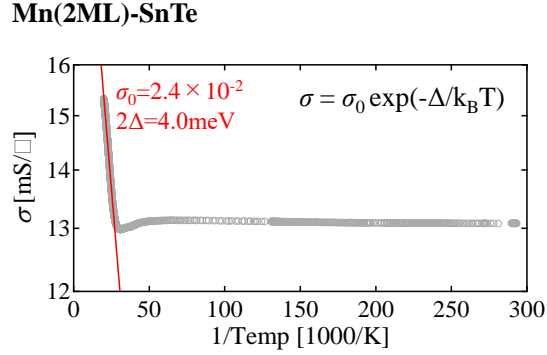


FIG S4. The conductivity ( $\sigma$ ) plotted as a function of the inverse of temperature for the data sets shown in Fig. 3(b). The solid lines show a fitting to Eq. (1).

Figure S4 shows the temperature dependence of the conductivity ( $\sigma = 1/R$ ) of Mn(2ML)-SnTe plotted as a function of the inverse temperature. To isolate the bulk and surface contributions to the conductivity at low temperatures, the data at 35-50 K were fitted using a simple thermal activation conduction model described by Eq. (1).

$$\sigma = \sigma_0 \exp\left(\frac{-\Delta}{k_B T}\right) \quad (1)$$

where  $\sigma_0$  is the pre factor and  $\Delta$  is the activation energy. The extrapolated conductivity down to 3 K was estimated to be 0.029 mS/□. In contrast, the actual conductivity at 3.5 K is 13 mS/□. The significantly higher conductivity compared to the value expected from bulk conduction in the 35-50 K range suggests a dominant contribution from surface states. Meanwhile, the slight increase in resistance observed below 10 K for Mn(2, 4ML)-SnTe (see Fig. 3(b, c)) can be attributed to weak localization effects in the two-dimensional metallic states [5].

[1] S. Fragkos, R. Sant, C. Alvarez, E. Golias, J. M. Velasco, P. Tsipas, D. Tsoutsou, S. A.-Giamini, E. Xenogiannopoulou, H. Okuno, G. Renaud, O. Rader, A. Dimoulas, “Topological band crossings in epitaxial strained SnTe”, *Phys. Rev. Mater* **3**, 104201 (2019).

[2] A. K. Pedersen, S. Ichinokura, T. Tanaka, R. Shimizu, T. Hitosugi, and T. Hirahara, Interfacial superconductivity in FeSe ultrathin films on SrTiO<sub>3</sub> probed by in situ independently driven four-point-probe measurements, *Phys. Rev. Lett.* **124**, 227002 (2020).

[3] K. Ide, T. Tanaka, A. Pedersen, S. Ichinokura, and T. Hirahara, Temperature dependence of the superconducting gap of single-layer FeSe/SrTiO<sub>3</sub>: Direct comparison between transport and spectroscopic measurements, *Phys. Rev. Mater.* **6**, 124801 (2022).

[4] K. Ishihara, S. Ichinokura, S. V. Ereemeev, T. T. Sasaki, R. Takada, H. Nishimichi, R. Akiyama, E. V. Chulkov, and T. Hirahara, Manipulation of the anomalous Hall effect in magnetic topological insulator

heterostructure  $\text{MnBi}_2\text{Te}_4$  /  $\text{Bi}_2\text{Te}_3$  by Si substrate surface engineering, *Appl. Phys. Lett.* **127**, 211601 (2025).

[5] G. Bergmann, Weak localization in thin films: a time-of-flight experiment with conduction electrons, *Phys. Rep.* **107**, 1 (1984).